PHYSICAL REVIEW B **103**, 014112 (2021)

Metamagnetic transitions and magnetoelectricity in the spin-1 honeycomb antiferromagnet $Ni_2Mo_3O_8$

Y. S. Tang,[1] J. H. Zhang,[1] L. Lin,[1,*] R. Chen,[2] J. F. Wang,[2] S. H. Zheng,[1] C. Li,[3,4] Y. Y. Zhang,[1] G. Z. Zhou,[1] L. Huang,[1]
Z. B. Yan,[1] X. M. Lu,[1] D. Wu,[1] X. K. Huang,[5] X. P. Jiang,[5] and J.-M. Liu[1]
[1]*Laboratory of Solid State Microstructures, Nanjing University, Nanjing 210093, China*
[2]*Wuhan National High Magnetic Field Center and School of Physics, Huazhong University of Science and Technology, Wuhan 430074, China*
[3]*Forschungszentrum Jülich GmbH, Jülich Centre for Neutron Science Outstation at SNS, Germany*
[4]*Oak Ridge National Laboratory, Oak Ridge, Tennessee 37831, USA*
[5]*School of Materials Science, Jingdezhen University of Ceramics, Jingdezhen 333403, China*

(Received 13 September 2020; revised 24 December 2020; accepted 11 January 2021; published 20 January 2021)

Earlier neutron scattering studies suggested the coexistence of complex stripelike and zigzaglike antiferromagnetic orders in polar honeycomb lattice $Ni_2Mo_3O_8$, while its magnetoelectric (ME) behavior as an emergent effect is thus of high interest. Here we report our observations of two metamagnetic transitions and novel ME responses of $Ni_2Mo_3O_8$ single crystals against high magnetic field H up to ∼60 T. The c-axis (polar axis) spontaneous electric polarization P_{spin}, emerging at the magnetic Néel temperature $T_N \sim 5.5\,\mathrm{K}$, and its remarkable response to H applied along the c axis ($H//c$) and a axis ($H//a$), respectively, provide the clear evidence for the magnetism-driven ferroelectricity. While the magnetism exhibits the in-plane anisotropy to some extent, the magnetic field dependencies of magnetization and electric polarization in the low-field region and high-field region are distinctly different. In the low-field region where a weak spin-flop type metamagnetic transition occurs, the electric polarization response shows the parabolic dependence of magnetic field applied along both the c axis and in-plane a axis. The second metamagnetic transition happens when the magnetic field extends up to the high-field region where the magnetization and electric polarization response at low temperature are characterized by an extraordinarily broad plateau for the magnetic field along the c axis but roughly linear dependence for field along the a axis. These unusual phenomena are discussed, based on the symmetry-related local ME tensor analysis, and it is suggested that both the spin current and p-d hybridization mechanisms may contribute to the spontaneous electric polarization and ME responses. The present work demonstrates $Ni_2Mo_3O_8$ as a unique multiferroic and promising platform for exploring the rich spin-1 physics and ME phenomena in honeycomb lattice.

DOI: 10.1103/PhysRevB.103.014112

I. INTRODUCTION

Multiferroics possessing more than one ferroic order parameter are of significant interest due to their potential application in novel electronic devices [1,2]. Among them, the fascinating interplay between the magnetization (M) or electric polarization (P) induced by electric field (E) or magnetic field (H), respectively, has attracted tremendous interest because of the strong magnetoelectric (ME) effect [3,4]. There are two types of multiferroics: in type-I multiferroics, the ferroelectricity and magnetism have different origins, and are largely independent of each other, whereas the magnetic order itself induces ferroelectricity in type-II multiferroics. Constrained by the symmetry requirements, very limited materials exhibiting strong ME coupling were found in the frustrated magnets. In particular, besides the cross coupling between ferroelectric and magnetic order, the observed topological phenomena associated with multiferroicity and magnetoelectric coupling has been intensively stimulated, such as the ME coupling in a skyrmion lattice [5], topological defects in hexagonal $YMnO_3$ [6], magnetoelectric monopole [7], the toroidal moment [8], and optical diode effect [9,10].

Along with continuing efforts to realize colossalization of the ME signal, as well as the subsequent phenomena associated with multiferroicity, some ME materials exhibiting novel metapolarization transition response along with the occurrence of metamagnetic transition (e.g., spin-flop, magnetization plateau) in the trigonal or kagome lattice, such as $CuFeO_2$ [11], $Ni_3V_2O_8$ [12], Ni_3TeO_6 [13], and $PbCu_3TeO_7$ [14], have strongly received the interest in this topic. It has been suggested that the strong next-nearest-neighbor and next-next-nearest-neighbor interactions may play important roles in promoting the formation of exotic magnetic orders [15–17]. One candidate of such ME materials is magnetic nickelates in spin-1 systems, e.g., $A_3Ni_2XO_6$ (A = Li, Na and X = Sb, Bi) [15], $Na_2Ni_2TeO_6$ [17], and $BaNi_2V_2O_8$ [18], in which various types of magnetically ordered states are established. Nonetheless, quite a few concerning the research about the ME coupling in the honeycomb-based materials with fascinating physics has been investigated [19,20].

---

[*] Corresponding author: llin@nju.edu.cn

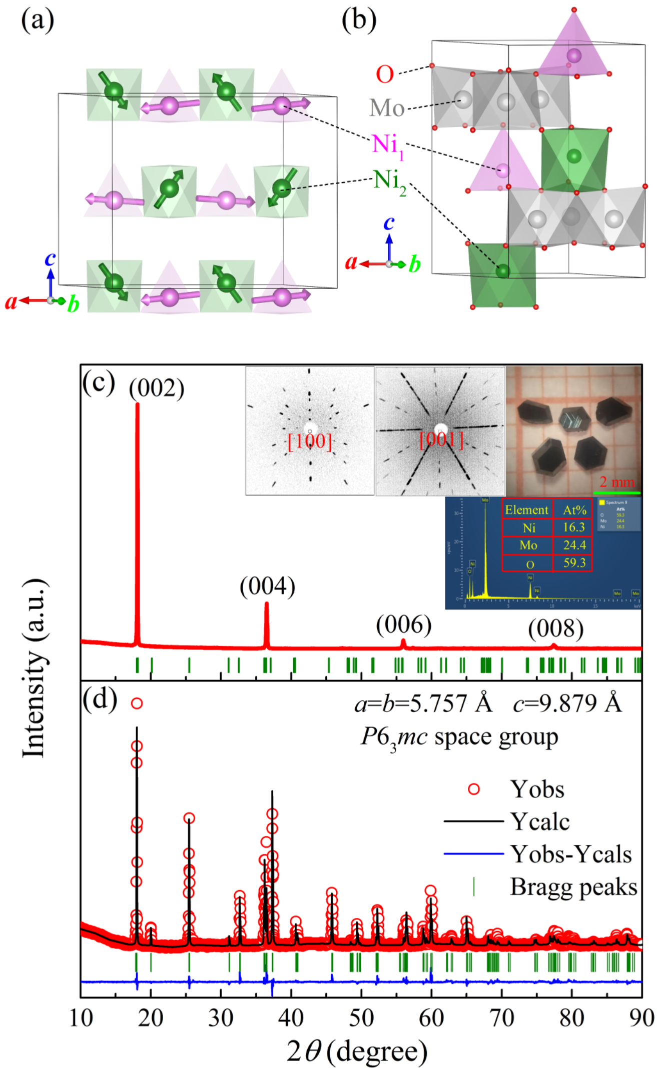

FIG. 1. (a) The schematic diagram of magnetic structure in $Ni_2Mo_3O_8$ with magnetic space group P_Cna2_1. The spins of the Ni_1 and Ni_2 sites are expressed in the magenta and green colors. (b) The crystal structure of $Ni_2Mo_3O_8$ with polar space group $P6_3mc$. (c) The XRD pattern of as-grown single crystal, and the insets show the image, Laue spots, and chemical component analysis of the crystals. (d) The XRD pattern of the $Ni_2Mo_3O_8$ powders at room temperature and the data from the corresponding Rietveld fitting.

Most recently, Morey and McQueen *et al.* reported more complex AFM order on a honeycomb lattice with a mixture of stripy and zigzag characters in polycrystalline $Ni_2Mo_3O_8$, as shown in Fig. 1(a) [21], which is essentially different from the trigonal or kagome lattice mentioned above. Compared to the other compounds in this $M_2Mo_3O_8$ (M = Fe, Mn, Co) family, $Ni_2Mo_3O_8$ looks different in terms of magnetic structure [22]. First, $Ni_2Mo_3O_8$ has an orthogonal magnetic structure (magnetic space group P_Cna2_1) in the ground state, while other members exhibit hexagonal magnetic structure. Second, it is suggested that the zigzag AFM order in $Ni_2Mo_3O_8$ may be stabilized by the bond-dependent anisotropic exchange due to ligand distortion, which usually appears in the 4*d* and 5*d* ions with strong anisotropy and spin-orbit coupling [15]. Third, such complex magnetic structure indicates the stronger second- and third-neighbor interactions in $Ni_2Mo_3O_8$ [23], similar to the honeycomb compounds α-$RuCl_3$, Li_2IrO_3, and Na_2IrO_3 that allow a Kitaev quantum spin liquid state to emerge [24–26].

In addition to these fundamental aspects, the most intriguing phenomena found in $M_2Mo_3O_8$ recently include the prominent magnetoelectric (ME) coupling between the magnetic and ferroelectric orders [27–30]. Crystallographically, $Ni_2Mo_3O_8$ lattice belongs to the noncentrosymmetric space group ($P6_3mc$) with Ni^{2+} ions occupying both the tetrahedral (Ni_1) and octahedral (Ni_2) sites, as shown in Fig. 1(b). It is noted that the Mo^{4+} ions appear to be nonmagnetic due to the trimerization [22]. The large linear ME effects have been reported in $Fe_2Mo_3O_8$ [27,28] and $Mn_2Mo_3O_8$ [29]. One of their interesting features is that the AFM ground state appears to be fragile and can be easily switched to the ferrimagnetic (FIM) state or spin-flop state by either external magnetic field or Zn/Fe doping, which leads to the sign inverse of the ME coefficient [27,29]. Much recently we also reported the similar collinear magnetic structure in $Co_2Mo_3O_8$, accompanied only with the second-order ME effect [30].

Although the electronic structures and ME effect of $(Fe, Mn, Co)_2Mo_3O_8$ were thoroughly investigated, it seems that no clear consensus on the microscopic origin of giant ME effect has been reached. The first-principles calculations suggest that oxygen ion displacements originated from the exchange striction in the AFM state underlie the observed giant ME coefficients [28]. Most recently, two scenarios based on the homogeneous distribution of Fe^{2+} ions among the tetrahedral and octahedral sites and charge disproportionation with somewhat exotic ionization state 1+ at the tetrahedral sites were proposed [23]. Here $Ni_2Mo_3O_8$ is a much more attractive case. First, different from the collinear order along the *c* axis in those $(Fe, Co, Mn)_2Mo_3O_8$ materials, the feature of coexistence of stripe and zigzag AFM order in $Ni_2Mo_3O_8$ is clear, which enables an effort in exploring the rich physics of integer spin on the honeycomb lattice. Second, the weak metamagnetic feature in polycrystalline samples suggests a low-lying (in field) magnetic phase transition [21], and hence measurements on single crystals are highly required to explore the metamagnetic transitions driven by magnetic field along different crystallographic directions, noting that the AFM orders along the *c* axis and in the *ab* plane are different [21]. Third, different from those $6'mm'$ (AFM) and $6m'm'$ (ferromagnetic) hexagonal magnetic point groups, the P_Cna2_1 orthogonal magnetic group allows nonlinear spiral spin order, which provides a platform to explore the potential novel physics beyond the linear ME coupling on a spin-1 honeycomb lattice [31].

Motivated by these discussions, it is unambiguous to reveal the ME coupling by combining the characterizations on magnetization, specific heat, and ferroelectric polarization of high-quality $Ni_2Mo_3O_8$ single crystals over a broad range of magnetic field *H* up to 60 T in this work. The magnetic phase transition, ME coefficient, and ME phase diagram are systematically investigated. In contrast to the other members of $M_2Mo_3O_8$ family, our results reveal the distinctly different magnetic and ME coupling behaviors in the low- and high-magnetic field regions. In the low-field region, the electric polarization response shows the parabolic dependence while the magnetic structure exhibits the clear spin-flop transitions. More intriguingly, over the high-field region, the magnetization and electric polarization response exhibit extraordinarily broad plateaus against magnetic field along the *c* axis but roughly linear dependence on magnetic field along the *a* axis. Therefore, $Ni_2Mo_3O_8$ stands out as a new exotic multiferroic in this $M_2Mo_3O_8$ family.

II. EXPERIMENTAL DETAILS

The single crystals of $Ni_2Mo_3O_8$ were grown using the chemical vapor transport technique as described earlier [32,33]. In detail, stoichiometric mixture of high-purity NiO and MoO_2 powder was thoroughly ground and sealed in evacuated silica tubes at 1000 °C for 48 h to synthesize polycrystalline $Ni_2Mo_3O_8$ powder. Then the obtained power and transporting agent $TeCl_4$ with molar ratio 14:1 were sealed in evacuated silica tubes at 1000 °C in the change zone (T_1) and 850 °C in the growth zone (T_2) for 15 days to grow the single crystals [photoimaged crystals are shown in Fig. 1(c)]. The crystal structure was characterized by x-ray diffraction (XRD) (D8 ADVANCE, Bruker) with CuK_α source ($\lambda = 1.5406$ Å). The back-reflection Laue detector (MWL120, Multiwire Laboratrories, Ltd.) was used to check the quality of obtained single crystals and determine the crystallographic orientation. The electron dispersion spectroscopy (EDS) (Quanta 200, FEI) was used to analyze the chemical composition.

The well-prepared and aligned samples were submitted for a series of characterizations. First, the temperature (T) dependence of magnetic susceptibility (χ) were measured using the Quantum Design Superconducting Quantum Interference Device magnetometer (SQUID) from 2 to 300 K under the zero-field-cooled (ZFC) and field-cooled (FC) conditions with cooling magnetic field $H = 0.1$ T. Simultaneously, the magnetization (M) as a function of H was measured at selected T. For high-H experiments, the in-plane and out-of-plane magnetizations were measured at selected T in the pulsed field mode, using a coaxial pickup coil and calibrated by a comparison with the low-field data measured by SQUID. The specific heat (C_p) data were collected from $T = 2$ to 20 K using the Quantum Design Physical Properties Measurement System (PPMS).

Resembling earlier reports, the electric polarizations were obtained by conventional pyroelectric current measurement [34], noting that no electric or magnetic poling of the sample is needed here, similar to $Fe_2Mo_3O_8$ [28]. The T dependence of pyroelectric current (J_c) was collected upon T increasing from 2 to 30 K using the Keithely 6514 programmable electrometer, with a sample warming rate of 4 K/min. In addition, to explore the ME coupling, the H-dependent magnetocurrent (J_m) with $H//a$ axis and $H//c$ axis modes were also recorded at a fixed T (∼2 K) upon H ramping from −9 to 9 T at a rate of 100 Oe/s. The variation in electric polarization (ΔP_c) was obtained by integrating the pyroelectric current with the time. In addition, the high field-induced ΔP_c was also measured in the $H//c$ and $H//a$ modes, noting that a small bias electric field $E = 1$ kV/cm was applied under the warming sequence to ensure the high-quality data. All the high-field data were measured using the 10.5 ms short-pulse magnet in the Wuhan National High Magnetic Field Center (WHMFC).

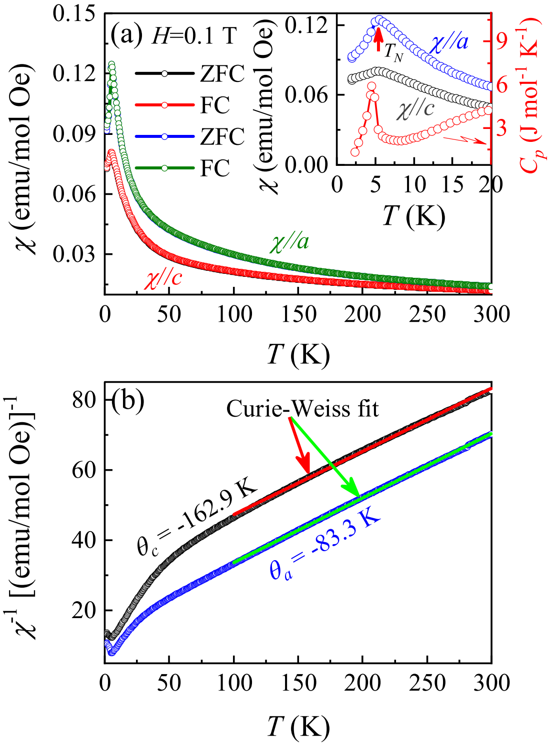

FIG. 2. (a) The measured magnetic susceptibility as a function of T, $\chi(T)$, and (b) the Curie-Weiss fitting χ^{-1} measured along the *c* axis and *a* axis, respectively. The inset shows the amplifying $\chi(T)$ curve and specific heat C_p details at low-T range.

III. RESULTS AND DISCUSSIONS

A. Crystal structure

In most cases, the as-grown crystals are naturally hexagonal in geometry, with ∼2 mm in diameter and 1.0 to 1.5 mm in thickness, as shown in the inset of Fig. 1(c). The room-temperature slow-scan XRD pattern onto the naturally developed hexagonal plane is presented in Fig. 1(c) too, which shows very sharp diffraction peaks well indexed by the (00l) reflections. In addition, such a hexagonal plane is aligned with the back-reflection Laue detector, showing perfect diffraction spots from the [001] direction, demonstrating the good quality of our crystals.

The refined structure of $Ni_2Mo_3O_8$ fits the noncentrosymmetric $P6_3mc$ space group with unit cell parameters $a = b = 5.757$ Å, $c = 9.879$ Å, in agreement with previously reported data from powder neutron scattering [21], as shown in Fig. 1(d). Furthermore, the as-grown crystals were checked for their chemical composition using the EDS technique, giving rise to the atomic Mo:Ni ratio of 24.4 : 16.3 = 1.4969, close to the nominal ratio 1.5. The high chemical and structural quality of the as-grown single crystals is confirmed.

B. Magnetic susceptibility and specific heat

We present the conventional characterizations on the DC magnetic properties. Figure 2(a) shows the measured $\chi(T)$ curves in the ZFC and FC modes with a measuring field of 0.1 T in the geometry aligned along the *c* axis and *a* axis, respectively. Several features deserve highlighting here. First, the $\chi(T)$ curves along the c axis ($\chi//c$) and a axis ($\chi//a$) show remarkable difference, noting that the shape anisotropy is negligible here. The larger in-plane susceptibility is consistent with the neutron scattering result [21], suggesting the in-plane Ni^{2+} spin anisotropy. Second, the two $\chi(T)$ curves increase with decreasing T and reach the peak at $T_N \sim 5.5$ K, the AFM Néel point, as highlighted in the inset of Fig. 2(a). This AFM transition is confirmed by the specific heat $C_p(T)$ curve presenting a typical λ-shaped anomaly (characteristic three-dimensional magnetic order) at $T_N \sim 5.5$ K, consistent with earlier data [21,35]. Third, the $\chi^{-1}(T)$ curves plotted in Fig. 2(b) unveil the dominant AFM interactions. By analyzing the data far above T_N (above 100 K), we find that the fitted Curie-Weiss temperature (θ) in the $H//c$ (θ_c) and $H//a$ (θ_a) geometries are -162.9 and -83.3 K, respectively, indicating the stronger AFM coupling along the c axis than the a axis. The derived effective paramagnetic moment μ_{eff} along the c axis and a axis are 3.33 and 3.30 μ_B/Ni. These values are between the expected value of spin-only moment (2.8 μ_B/Ni) and total effective moment (5.6 μ_B/Ni), implying the incomplete orbital moment quenching. Finally, the frustration ratio (f) along the two directions can be estimated too, giving rise to $f = \theta/T_N \sim 29.6$ for the $H//c$ case and ~15.1 for the $H//a$ case, indicative of the stronger magnetic frustration in the c direction.

Here it should be mentioned that both the θ and μ_{eff} values extracted from our single crystals are slightly different from those from the polycrystalline samples [21], and such difference can be reasonably attributed to the possible imperfections and random grain orientations with the polycrystalline samples. Indeed, a tiny amount of $NiMoO_4$ impurity phase was found in the polycrystalline samples, as revealed by the powder neutron diffraction [21].

C. Low-field magnetization

Based on the $\chi(T)$ data, it is concerning how magnetization M as a function of H evolves. We focus on the M responses to H in the $H//c$ and $H//a$ modes below T_N, namely $M_a(H)$ and $M_c(H)$. We discuss the data in the low-field and high-field regions to be defined below. The data in the low-field region are displayed in Figs. 3(a) and 3(c) for the $H//c$ and $H//a$ cases.

In the low-field region, the typical AFM responses are observed, characterized by the roughly linear increasing of the $M_a(H)$ and $M_c(H)$ curves with H. Nevertheless, slight deviations from the linear dependencies reflect the spin-flop events. For the $M_c(H)$ data, such a deviation is marked by a small but clear jump at $H = H_{\text{low}}$, as shown in Fig. 3(a) and further illustrated by the sharp (dM_c/dH) peak in Fig. 3(b). This jump suggests the H-driven spin-flop event and it marks a metamagnetic transition often observed in transition metal oxides of the complicated AFM orders, where H_{low} is the critical field for such metamagnetic transition. For the $M_a(H)$ data, an obvious but weaker deviation from the linear dependence can be found at $T = 2$ and 3 K, as shown in Fig. 3(d), indicating a metamagnetic transition induced by the field. The critical field H_{low} for the $H//c$ cases are larger than that for the $H//a$ cases, and they evidently decrease with increasing T and disappear at $T_N \sim 5.0$ K.

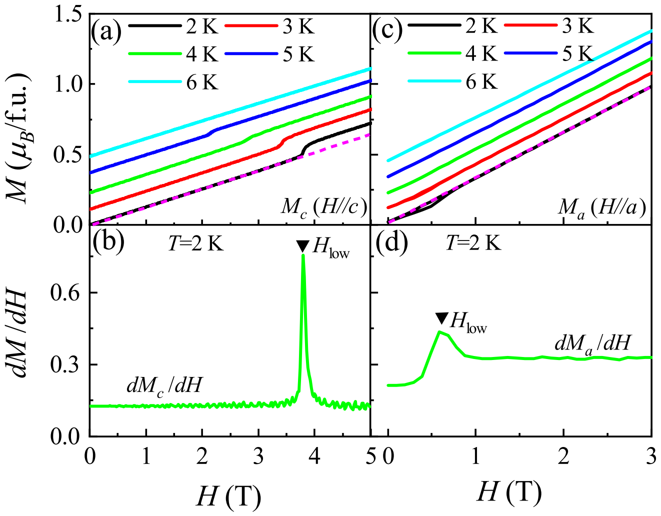

FIG. 3. The low-field magnetization M of $Ni_2Mo_3O_8$. The magnetic field dependence of the magnetization with $H//c$ and $H//a$, namely (a) $M_c(H)$ and (c) $M_a(H)$ measured at selected temperatures. (b) and (d) Derivative of the magnetization dM_c/dH and dM_a/dH with respect to the magnetic field for fields $H//c$ and $H//a$ measured at $T = 2$ K.

D. High-field magnetization

Extending the measuring up to the high field region (pulse field events) unveiled some different characters, and an overall illustration of the $M_a(H)$ and $M_c(H)$ data are plotted in Figs. 4(a) and 4(c) where the low-field data from the SQUID

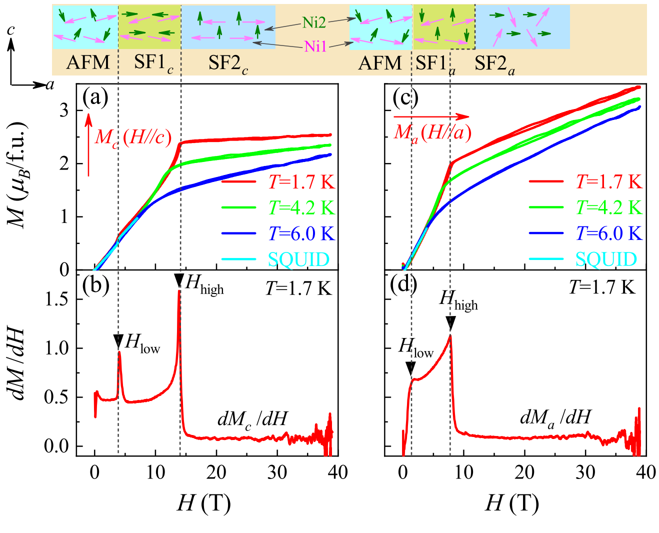

FIG. 4. The high-field magnetization of $Ni_2Mo_3O_8$. The H dependence of the magnetization (a) $M_c(H)$ with $H//c$, and (c) $M_a(H)$ with $H//a$ under selected T. (b) and (d) Derivative of the magnetization dM_c/dH and dM_a/dH with respect to the magnetic field for fields $H//c$ and $H//a$ measured at $T = 1.7$ K, respectively. The speculated spin arrangements located in the antiferromagnetic (AFM) phase, low-field spin-flop ($SF1_a$ and $SF1_c$) phase, and high-field spin-flop ($SF2_a$ and $SF2_c$) phase with $H//c$ and $H//a$ are plotted on the top of the figure. The magenta arrow stands for the Ni_1 (tetrahedral site), and the green arrow denotes the Ni_2 (octahedral site).

measurement are inserted for comparison. It is seen that the spin-flop feature is evident in both the low-field SQUID data and pulse-field data on $M_c(H)$ and $M_a(H)$, confirming the data reliability. Besides the spin-flop jump at critical field H_{low} in the low-field region, another clear metamagnetic transition occurring at critical field H_{high} is observed for both the $H//c$ and $H//a$ cases, respectively. The metamagnetic transitions can be more clearly identified in the (dM/dH) curves in Figs. 4(b) and 4(d), noting that the critical field (H_{high}) is used to define the low-field region and the high-field one in the present work.

Again, several features from the $M(H)$ data deserve highlighting, taking the $M_c(H)$ data as an example. First, two metamagnetic transitions occurring at $H_{\text{low}} = 4.0\,\text{T}$ and $H_{\text{high}} = 13.8\,\text{T}$ for $T = 1.7\,\text{K}$ are unambiguously evidenced. Second, above H_{high}, a clear and broad $M_c(H)$ plateau ranging from H_{high} beyond 40 T is demonstrated at $T = 1.7\,\text{K}$. It is noted that the saturation value for this system would be $\sim 5.9\,\mu_B/\text{f.u.}$ estimated from the ESR measurement on polycrystalline samples [21]. This plateau magnetization ($\sim 2.5\,\mu_B/\text{f.u.}$) is about half of the saturation value, indicative of the 1/2-like plateau. Third, with increasing T, both H_{low} and H_{high} move to the low field side and the 1/2-like plateau becomes dim and almost disappeared near T_N. Similar but much more vague features can be found from the $M_a(H)$ data. While the two metamagnetic transitions occurring at relatively low fields can be identified, as shown in Figs. 4(c) and 4(d), the magnetization plateau feature is far from clear and the high-field magnetization M_a shows somehow linear increasing with H beyond 40 T.

While the two metamagnetic transitions are evidenced, the spin structure evolutions remain not well defined so far. As for the metamagnetic transition at $\sim H_{\text{low}}$, the discussion on the polycrystalline samples suggests the conventional low-lying (in field) magnetic transition, which could be interpreted as differences between the in-plane and out-of-plane magnetic responses, is confirmed by our data on single crystals. Spin-flop transition as one classical effect describes the magnetic field-driven first-order reorientation transition in some easy-axis antiferromagnets. In $Ni_2Mo_3O_8$, the magnetic moments of the tetrahedral Ni_1 (in magenta color) and the octahedral Ni_2 (in green color) are 2.64 and 1.68 μ_B, respectively. While the AFM interaction and spin frustration along the c axis are much stronger, here we assume that Ni_1 spins exhibit the stronger exchange interaction due to the larger moment, so that the spins on the Ni_1 sites are much more robust against the magnetic field than that on the Ni_2 sites.

In this case, for the low-field spin-flop transition, the c-axis field will cause a rotation of spins on the octahedral Ni_2 site away from the easy axis (c axis), while the spins on the tetrahedral Ni_1 site do not necessarily reorientate owing to the relatively large moment and weak magnetic field. However, the nearest-neighbor Ni_1-Ni_1, Ni_2-Ni_2, and the next-nearest-neighbor Ni_1-Ni_2 along c axis still prefer the AFM interaction, as featured on the top of Fig. 4(a) by the schematic drawing of the spin structure. Similar to the discussion above, the a-axis field will cause a rotation of spins on the octahedral site away from the a-axis direction, in the low field range, noting that the Ni_1-Ni_1, Ni_2-Ni_2 pairs still prefer the AFM interaction. Due to the strong AFM interaction along the c axis, the critical field for spin-flop should be larger for M_c, consistent with our experimental finding that both H_{low} and H_{high} for $H//c$ cases are larger than those for $H//a$ cases, respectively. In addition, there is a large difference in susceptibility between a longitudinal and transverse field, evidenced by dM_a/dH at AFM and SF1_a phases in Fig. 4(d). Exactly, $Ni_2Mo_3O_8$ exhibits an ordered magnetic state characterized as an admixture of stripy and zigzag order in the ab plane and c direction, respectively. In the c direction, the zigzag AFM order may be stabilized by a bond-dependent anisotropic exchange due to ligand distortion as reported in the $Ni_2Mo_3O_8$ polycrystalline [21]. Such a complex AFM order may lead to the anisotropy of the exchange interaction between the ab plane and c direction. These similar behaviors can be seen in other ME materials, such as the $Ni_3V_2O_8$ [12].

However, it should be mentioned that the details of magnetic structures in responding to the high-lying spin-flop (SF2_a and SF2_c) transition at $H \sim H_{\text{high}}$ remain unclear and require more experiments to verify, such as neutron scattering experiments applied in magnetic field. Nevertheless, this does not prevent us from tentative explanation by combining the data on magnetization and field-induced polarization, which will be discussed in detail later. To this end, the low-field and high-field magnetizations are revealed to show distinctly different behaviors, benefiting to our understanding of the ME coupling while the ME responses in the low-field and high-field regions are also distinctly different. Subsequently, we turn to the main issue and discuss the ME responses in these two regions separately.

E. Low-field ME effect

$Ni_2Mo_3O_8$ has the same polar structure as other $M_2Mo_3O_8$ systems and thus the most concerned issue is the ferroelectricity and ME coupling. Here the reason that we choose the c axis as the orientation along which the magnetoelectric coupling was measured, is that only the c-axis spontaneous polarization constrained by the $P6_3cm$ lattice space group and P_Cna2_1 magnetic space group is allowed. Of course the ME tensors could also give rise to polarization along a axis, while unfortunately this is not investigated in this work. We do observe the emergence of pyroelectric current and thus electric polarization (P_{spin}) along the c axis but no other signal along the a axis (and b axis) in zero magnetic field. Our attention will be then paid to the polarization variation ΔP_c against $H//c$ axis and $H//a$ axis, respectively. For details, we present in Figs. 5(a) and 5(b) the pyroelectric current J_c and the evaluated P_{spin} as a function of T in the absence and presence of magnetic field. For $H = 0$, there is a sharp J_c peak emerging at T_N, indicating magnetic ordering-induced polarization, defining the ferroelectric transition point $T_{\text{FE}} \sim T_N$. With increasing H, one observes an evident shift of T_{FE} and suppression of P_{spin}, giving rise to ΔP_c. This suppression is more pronounced as $H//a$ than that as $H//c$.

It is seen that P_{spin} for $Ni_2Mo_3O_8$ is $\sim 290\,\mu\text{C/m}^2$ $T = 2\,\text{K}$, much smaller than the values observed in single crystals of $Fe_2Mo_3O_8$ ($\sim 1400\,\mu\text{C/m}^2$) [27], $Mn_2Mo_3O_8$ ($\sim 2000\,\mu\text{C/m}^2$) [29], and $Co_2Mo_3O_8$ ($\sim 1200\,\mu\text{C/m}^2$) [30]. Such large difference becomes reasonable if one notices the specific noncollinear magnetic structure of $Ni_2Mo_3O_8$,

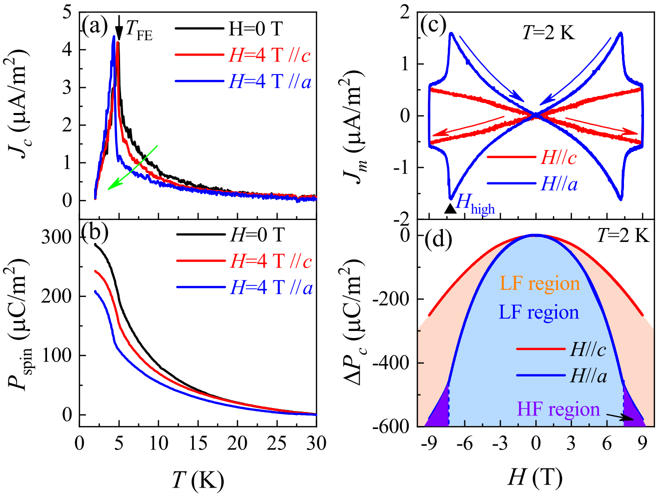

FIG. 5. The T-dependent (a) pyroelectric current density (J_c) and (b) change of ferroelectric polarization (P_{spin}) against $H//c$ axis and $H//a$ axis. The H dependence of (a) magnetocurrent density (J_m) and variation of polarization (ΔP_c) against $H//c$ axis and $H//a$ axis at $T = 2$ K.

while other members share the collinear spin order. In fact, consulting with the well-established experimental facts and microscopic mechanism for type-II multiferroics, one understands that the spiral spin order induced electric polarization, associated with spin-orbit coupling, is generally small but the ME effect is usually remarkable, because the noncollinear spin order is more flexible against external stimuli. On the contrary, the symmetric exchange striction-induced polarization, essentially observed in materials with collinear spin order, can be much larger.

Regarding the ΔP_c as a function of H, i.e., the ME response, remarkable variation occurs for both the $H//c$ and $H//a$ cases. In detail, one sees from Fig. 5(c) the magnetocurrent density (J_m) response against $H//c$ and $H//a$, respectively. Here the $J_m(H)$ data are collected by sweeping the magnetic field from positive to negative and then back to positive at $T = 2$ K, as denoted by arrows in Fig. 5(c). Obviously there exists a significant difference between the ME effects for the $H//c$ and $H//a$ cases. For the $H//c$ case, J_m varies in a nearly linear behavior in response to the field, while the response for the $H//a$ case exhibits a much stronger nonlinear character. It should be mentioned that the butterflylike ME loop for the $H//a$ case, distinctly different from the $H//c$ case, is more or less related to the metamagnetic transition occurring at $H \sim H_{\text{high}}$.

The evaluated $\Delta P_c(H)$ data are plotted in Fig. 5(d), and the ΔP_c at $H = 9$ T can be as large as -250 and $-578\,\mu$C/m^2 for the $H//c$ and $H//a$ cases, respectively. This consequence is surprising since $\Delta P_c(H)$ can be one and two times larger than P_{spin}, quite unusual for multiferroic materials and other M_2Mo$_3$O$_8$ members in which the H-modulated ΔP_c is much smaller than P_{spin} itself. As expected from the magnetic space group, the $\Delta P_c(H)$ behaviors for the $H//c$ and $H//a$ cases should follow the parabolic dependence, confirmed by the data in Fig. 5(d). In addition, the spin-flop triggered by $H \sim H_{\text{high}}$ is accompanied by a structural transition indicated by the deviation of $\Delta P_c(H)$ from the quadratic dependence.

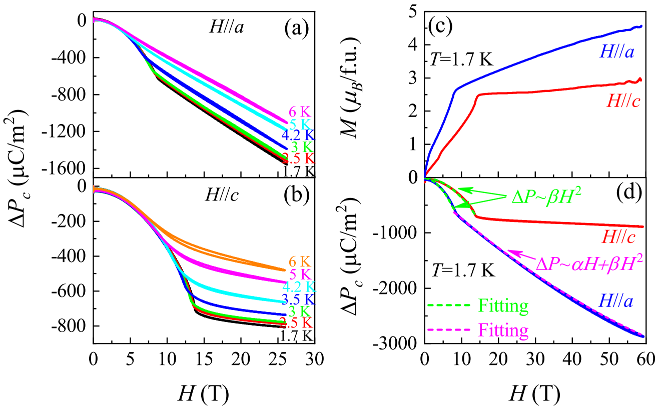

FIG. 6. (a) and (b) The polarization (ΔP_c) with respect to the magnetic field for fields $H//a$ and $H//c$ up to 26 T measured at $T = 1.7$ K, respectively. (c) The $M_a(H)$ and $M_c(H)$ curves measured at $T = 1.7$ K with H up to 60 T. (d) The H-dependent polarization ΔP_c at $T = 1.7$ K with $H//a$ and $H//c$ up to 60 T. The dashed bright green lines and dashed magenta curve are the fits to the ΔP-H curve with the different functions of $\Delta P \sim \beta H^2$ and $\Delta P \sim \alpha H + \beta H^2$, where α and β are constants.

It is worth reminding that the consistency in the phase boundary between the $M(H)$ and $\Delta P(H)$ curves indicates the strong correlation between magnetism and ferroelectricity, and the anisotropic ME coupling effect is thus reasonably demonstrated. We thus transfer to the discussion of the high-field ME effect since it must be different from the low-field behavior.

F. High-field ME effect

Moving to the experimental results obtained at the Wuhan High Magnetic Field Laboratory, the measured $\Delta P_c(H)$ curves for the $H//a$ and $H//c$ cases at several selected T were collected. We first look at the data for H up to 26 T, as plotted in Figs. 6(a) and 6(b), respectively. While the data in the low-field regions reproduce the results in Fig. 5, the typical parabolic dependencies in the low-field region are clearly shown. We then pay more attention to the high-field region where the dependencies are quite different and exhibit the roughly linear behaviors with the one-to-one correspondences between $\Delta P_c(H)$ and $M_c(H)$. Especially plateaulike $\Delta P_c(H)$ and $M_c(H)$ features emerge for $H//c$ at low T, as shown in Figs. 6(b) and 6(c) for $T = 1.7$ K. Therefore, an intrinsic coupling between the electric polarization and magnetization is also confirmed in the high-field region.

It is found that the low-$T\Delta P_c$ for $H//a$ case is $\sim -1600\,\mu$C/m^2 at $H \sim 26$ T, almost twice as that in $H//c$ case, displaying the dramatic ME anisotropy. It is known that the M plateau is an ordinary phenomenon typically born in frustrated nonpolar materials [36–38], nonetheless the coexistence of M plateau and P plateau in single-phase multiferroics is rather rare [14,39]. To the best of our knowledge, only the spin-1/2 honeycomb lattice antiferromagnet Cu$_2$(pymca)$_3$(CTlO$_4$) with the $P31m$ polar space group was reported to exhibit similar behavior [40]. Thus, Ni$_2$Mo$_3$O$_8$ seems to be a good platform for exploring the rich physics of integer spin on the honeycomb lattice. In addition, the plateaulike features seems to be persistent over a very broad region beyond $H \sim 60$ T, the limit of our measuring instrument, as shown in Figs. 6(c) and 6(d), respectively, indicating the considerable robustness of the AFM order along the c axis. For the $H//a$ case, both M_a and ΔP_c continue to increase linearly with increasing H, noting that the saturated magnetization is $\sim 5.9\,\mu_B/\mathrm{f.u.}$ [21].

To present a quantitative measure of the ME effect, the ME coefficients are evaluated from the $\Delta P_c(H//a)$ and $\Delta P_c(H//c)$ data. In general, the $\Delta P_c(H)$ is expressed as a polynominal up to the second order:

$$\Delta P_c = P_c - (P_{\mathrm{latt}} + P_{\mathrm{spin}}) = \alpha H + \beta H^2, \qquad (1)$$

where P_{latt} is the lattice-related spontaneous polarization [29], and α and β are the first-order and second-order ME coefficients, respectively.

It is already shown in Fig. 5(d) that the $\Delta P_c(H)$ curves below H_{high} show prefect quadratic fittings to H, as confirmed by the dashed bright green curves in Fig. 6(d), concomitance with the fact that the magnetic space group (P_Cna2_1) allows only the second-order ME coupling, while the linear ME effect is forbidden. In the low-field region, the fitted $\beta_{H//a} \sim -1.3 \times 10^{-17}$ s/A and $\beta_{H//c} \sim -5.1 \times 10^{-18}$ s/A are obtained in the low T. These values are much larger than those found for $Fe_2Mo_3O_8$ (1.81×10^{-28} s/A) and $Co_2Mo_3O_8$ (2.9×10^{-18} s/A). We are more interested in the high-field region. For the $H//c$ cases, $\Delta P_c(H//c)$ exhibits the plateaulike behavior and the ME coefficients must be small or negligible. The $\Delta P_c(H//a)$ data in the high-field region can be well fitted by including the linear and H^2 terms, as denoted as the dashed magenta curve in Fig. 6(d) for $T = 1.7$ K. The best-fitted ME coefficients are $\alpha_{H//a} \sim -70$ ps/m and $\beta_{H//a} \sim 1.5 \times 10^{-19}$ s/A, confirming that $\beta_{H//a}$ is indeed negligible. The linear ME coefficient $\alpha_{H//a}$ is much larger than those typical linear ME compounds, including Cr_2O_3 ($\alpha \sim 4.13$ ps/m) [41], $Fe_2Mo_3O_8$ ($\alpha \sim 16.2$ ps/m) [27], $GaFeO_3$ ($\alpha \sim 21$ ps/m) [42], Fe_2O_3 ($\alpha \sim 50$ ps/m) [43], and $NdCrTiO_5$ ($\alpha \sim 2.01$ ps/m) [44].

Such a large linear ME response seems to be unusual and we argue that it originates from the strong ME coupling due to the lattice distortions associated with the octahedral and tetrahedral coordination environments modified by high magnetic field [21]. This is not surprising and we recall previous reports on typical linear ME magnet $LiMPO_4$ ($M =$ Mn, Fe, Co, Ni) where the important role of orbital moment contributions to the ferroelectricity was confirmed [45]. Hence, $Ni_2Mo_3O_8$ is a peculiar multiferroic that is distinct to other $M_2Mo_3O_8$ members.

G. ME phase diagram

All the presented results are sufficient for us to draw the ME phase diagrams, as shown in Figs. 7(a) and 7(b), respectively. The phase regions are separated by the peak positions in the dP/dH, dM/dH, T_N (and also T_{FE} in Fig. 5) as a function of H at various temperatures. The low-T AFM ground state is separated from the paramagnetic (PM) phase in the high-T range by the AFM Neel point T_N that is also the magnetic ordering point in the presence of magnetic field H. Our magnetization data show that this ordering point does not change much against magnetic field up to ∼30 T, suggesting the vertical boundary between the PM phase and low-T ordered phases, as shown in Fig. 7.

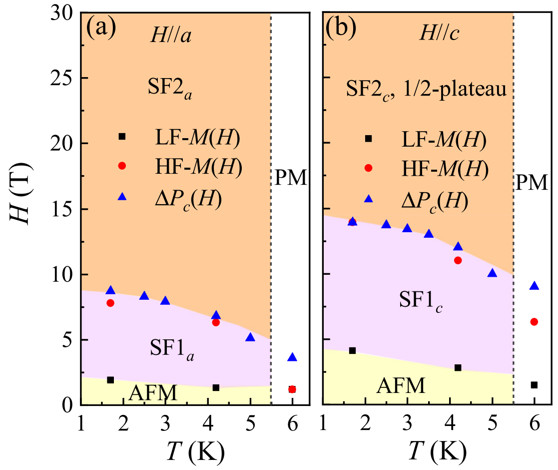

FIG. 7. The H-T magnetoelectric phase diagram of $Ni_2Mo_3O_8$ for (a) $H//a$, and (b) $H//c$ conditions. The results from low-field magnetization (LF)-$M(H)$, high-field magnetization (HF)-$M(H)$, and magnetic field response to polarization $\Delta P_c(H)$ were used to determine the phase boundary.

In the low-T phase regions, the AFM ground state and low-field spin-flopped ($SF1_a$ and $SF1_c$) phase are separated by H_{low}, as shown in Figs. 3 and 4. The high-field phase ($SF2_a$ and $SF2_c$) and the low-field phase are separated by H_{high}. These separating points constitute the phase boundaries, contributing to the phase diagrams shown in Fig. 7. It is also clearly shown that the phase diagrams for the $H//c$ and $H//a$ cases are quite different, the consequence of magnetic anisotropy.

IV. DISCUSSION

Finally, we present an updated discussion of the underlying mechanisms for the observed ME responses. On one hand, the c-axis spontaneous polarization emerging exactly at the AFM Néel point T_N ($\sim T_{\mathrm{FE}}$) confirms again $Ni_2Mo_3O_8$ as a type-I multiferroics [46,47], implying that the microscopic origin for ferroelectricity and ME responses should be relevant with one of the three possible mechanisms: (1) the spin-current mechanism for noncollinear spin order [48], (2) the exchange striction for collinear magnetic structure [49], and (3) the p-d hybridization mechanism between spin and its ligand atoms with spin-orbital interaction [50]. Nevertheless, the experimental data available to us are not sufficient to identify which mechanism, the Dzyaloshinskii-Moriya (DM) interaction, single-ion anisotropies, or both, are responsible for the noncollinear spin structure, although it is known that the spins on the octahedral and tetrahedral sites form stripy and zigzag AFM character in the ab plane and c axis, respectively, as presented in Fig. 8(a).

In proceeding, we may employ the recently developed symmetry-based local ME tensor technique to discuss the microscopic origin of polarization [51,52]. $Ni_2Mo_3O_8$ possesses the polar lattice symmetry and polar magnetic space

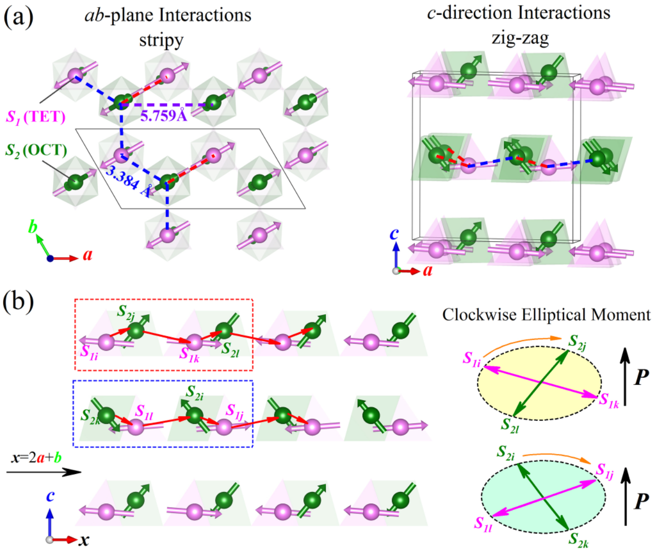

FIG. 8. (a) The schematically stripy *ab* plane and zigzag *c*-direction components of the magnetic structure of $Ni_2Mo_3O_8$. The spins on each tetrahedral and octahedral sites are plotted in light magenta and olive arrows. Nearest neighbor antiferromagnetic and ferromagnetic interactions are expressed in red and blue dashed lines, and the distance Ni_1-Ni_2 is 3.384 Å and the Ni_1-Ni_1/Ni_2-Ni_2 bonds have the length of 5.759 Å. (b) The sketch of cycloidal spiral order along $2\boldsymbol{a}+\boldsymbol{b}$ and c direction. Black arrows denote directions of ferroelectric polarization arising from the DM interaction. The red arrows represent unit vector pointing from the nearest neighbor site $1i$ to site $2j$.

group P_Cna2_1, imposing severe symmetric constraints over the forms of local ME tensors. We start from the consideration of the nearest-neighbor and next-nearest-neighbor exchanges, as plotted in Fig. 8(a) where the nearest-neighbor distance Ni_1-Ni_2 is 3.384 Å and the Ni_1-Ni_1/Ni_2-Ni_2 bonds have the length of 5.759 Å. A consideration of the three types of Ni-Ni bonds should be sufficient for discussing the local electric dipoles. The total polarization generated in the Ni_1-Ni_2 layer, pNi$_1$-Ni$_2$, by the two Ni_1-Ni_2 nearest-neighboring interactions, can be expressed as

$$p_{\text{Ni1-Ni2}} = \sum_{\langle i,j\rangle} P_{ij}^{\alpha\beta\gamma} S_{i\alpha} S_{j\beta} = \left(\sum_{\langle i,j\rangle} P_{i,j}^{\alpha\beta\gamma}\right) S_{1\alpha} S_{2\beta}, \tag{2}$$

where $\langle i, j\rangle$ runs all the adjacent Ni_1-Ni_2 pairs; (α, β, γ) runs over all the Cartesian coordinates, $\boldsymbol{x} = 2\mathbf{a} + \mathbf{b}$, $\boldsymbol{y} = \mathbf{b}$, $\boldsymbol{z} = \mathbf{c}$. The magnetic point group is $mm2$, which is polar and allows for the second-order ME effect. Based on the theoretical analysis of two-spin tensor ${P_{12}}^{\alpha\beta\gamma}$ in the 32 point groups [52], we can obtain the Ni_1-Ni_2 two-spin tensor ${P_{12}}^{\alpha\beta\gamma}$ as

$$\begin{aligned} P_{12}^{\alpha\beta\gamma} &= \begin{pmatrix} 0, 0, P_{12}^{xx(z)} & 0, 0, 0 & P_{12}^{xz(x)}, 0, 0 \\ 0, 0, 0 & 0, 0, P_{12}^{yy(z)} & 0, P_{12}^{yz(y)}, 0 \\ P_{12}^{zx(x)}, 0, 0 & 0, P_{12}^{zy(y)}, 0 & 0, 0, P_{12}^{zz(z)} \end{pmatrix} \\ &= \begin{pmatrix} 0, 0, f & 0, 0, 0 & f, 0, 0 \\ 0, 0, 0 & 0, 0, g & 0, g, 0 \\ h, 0, 0 & 0, k, 0 & 0, 0, l \end{pmatrix}, \end{aligned} \tag{3}$$

where f, g, h, k, l are the constants. Here the $(0, 0, l)$, $(f, 0, 0)$, and $(0, g, 0)$ denote vectors along the z, x, and y axis. For the zero field case, coefficient $l \neq 0$, allowing a local spontaneous polarization $p_{\text{Ni}_1\text{-Ni}_2}$ appearing in the z axis due to the nonzero components of Ni_1 and Ni_2 spins along the z axis, as shown in Figs. 8(a) and 8(b). For $H//x$ or $H//y$, the pNi$_1$-Ni$_2$ in the z axis can also be induced by the two-spin tensor h or k, consistent with our experiments where nonzero $\beta_{H//a} \sim -13 \times 10^{-18}$ s/A and $\beta_{H//c} \sim -5.1 \times 10^{-18}$ s/A in the AFM ground state were obtained.

For the Ni_1-Ni_1 and Ni_2-Ni_2 cases, the same form for tensor $P_{12}^{\alpha\beta\gamma}$ can also be exactly derived. From Eq. (2), the local polarization can be expressed in a form similar to the spin-current mechanism shown in Fig. 8(b):

$$p_{\text{Ni1-Ni2}} \propto e_{12} \times (S_1 \times S_2), \tag{4}$$

here S_1 and S_2 are the spins on tetrahedral and octahedral sites, and vector e_{12} denotes the connection from S_1 to S_2. In the framework of the spin-current model, one sees that the tetrahedral nickel carrying larger moment (1.727 μ_B) which lies mainly in the ab plane, and the moment (1.431 μ_B) on the octahedral site primarily points in the c axis [21]. Therefore, a cycloidal spiral spin order propagating along direction $\boldsymbol{x} = 2\boldsymbol{a} + \boldsymbol{b}$ is explicitly demonstrated, as shown in Fig. 8(b). Here the spins on one cycloidal chain (highlighted in red and blue dashed rectangle) are labeled as S_{1i}, S_{2j}, S_{1k}, and S_{2l}, and thus ferroelectric polarization $P \sim e_{ij} \times (S_{1i} \times S_{2j})$ could be induced along the c axis by breaking the inversion symmetry via the antisymmetric DM interaction [53]. Recently, a theoretical work using the effective spin model also confirmed the role of the DM interaction in developing the noncollinear spin order [54] and thus the ME coupling effect in $Ni_2Mo_3O_8$.

Besides the DM interaction, one may also discuss the single-spin induced ferroelectric polarization p_{Ni}. It can be written as

$$p_{\text{Ni}} = \sum_i P_{ii}^{\alpha\beta\gamma} S_{1\alpha} S_{1\beta} + \sum_j P_{jj}^{\alpha\beta\gamma} S_{2\alpha} S_{2\beta}, \tag{5}$$

where S_1 spin and S_2 spin reside on the i sites and j sites, respectively. Based on the symmetry restriction, the Ni_1 and Ni_2 single-spin tensors $P_{ii}^{\alpha\beta\gamma}$ and $P_{jj}^{\alpha\beta\gamma}$ can be deduced as

$$\sum_i P_{ii}^{\alpha\beta\gamma} = A \begin{pmatrix} 0, 0, P_{ii}^{xx(z)} & 0, 0, 0 & P_{ii}^{xz(x)}, 0, 0 \\ 0, 0, 0 & 0, 0, P_{ii}^{yy(z)} & 0, P_{ii}^{yz(y)}, 0 \\ P_{ii}^{zx(x)}, 0, 0 & 0, P_{ii}^{zy(y)}, 0 & 0, 0, P_{ii}^{zz(z)} \end{pmatrix}, \tag{6}$$

$$\sum_j P_{jj}^{\alpha\beta\gamma} = -B \begin{pmatrix} 0, 0, P_{jj}^{xx(z)} & 0, 0, 0 & P_{jj}^{xz(x)}, 0, 0 \\ 0, 0, 0 & 0, 0, P_{jj}^{yy(z)} & 0, P_{jj}^{yz(y)}, 0 \\ P_{jj}^{zx(x)}, 0, 0 & 0, P_{jj}^{zy(y)}, 0 & 0, 0, P_{jj}^{zz(z)} \end{pmatrix}, \tag{7}$$

where A and B are constants, corresponding to the different magnitude of moment between Ni_1 and Ni_2. It is obvious that polarization $p_{\text{Ni}} \neq 0$ at $H = 0$ due to the constants $A \neq B$. In addition, no matter in which direction H is applied (x, y, or z axis), the single-spin tensor from the two spin sites will no longer cancel each other out, e.g., $(A \cdot P_{ii}^{zz(z)} - B \times P_{jj}^{zz(z)}) \neq 0$, leading to all allowed nonzero spontaneous polarization components and ME coefficients, consistent with our experimental results shown in Figs. 6(a) and 7(d). Therefore, the p-d hybridization mechanism corresponding to the single-spin mode can also qualitatively explain our observations. In such sense, the *p-d* hybridization mechanism and the spin-current model may both contribute to the ferroelectric polarization P_{spin} and the ME responses $\Delta P_c(H)$.

Surely it should be mentioned that a quantitative estimation of the polarization and ME responses is essentially hindered by the complex mathematical handling for the two-spin and single-spin ME tensors, and the discussion presented here is more or less the consequence of a number simplifications. Honestly, it is beyond our ability to determine the specific magnetic space groups of the different magnetic phases in the present case that is too much challenging, unless neutron scattering experiments in applied magnetic field or rigorous calculations can resolve the magnetic structure. Nevertheless, this does not prevent us from tentative explanation by combining the data on magnetization and field-induced polarization.

The powder neutron diffraction suggests that the ground state belongs to the 33.154 (P_Cna2_1) magnetic space group [21]. While the magnetic space group describes all the possibilities of atoms, it becomes far more complex to track. Here it is more convenient to use magnetic point group $mm2$ to describe the magnetic structure P_Cna2_1. It is well known that by adding the time reversal symmetry operation, the magnetic point group $mm2$ can include four point groups: $mm2$, $mm2'$, $mm'2'$, *and* $m'm'2$, in which the first and second m denote mirror symmetry operation perpendicular to the y axis, and including the y axis, respectively. Here $2'$ represents a double rotational symmetry operation plus a time reversal symmetry operation. Because the antiferromagnetic order in the c direction creates time reversal symmetry, and the in-plane mirror-symmetric antiferromagnetism cannot constitute time reversal symmetry, it is much more accurate to describe the ground state by point group $mm2'$. Following up aforementioned symmetry analysis, we will focus our attention on speculating the magnetic point groups upon the SF transitions.

First, let us discuss the case of $H//c$. As discussed above, we could speculate that only Ni_2 spins change their directions to be perpendicular to the c axis, while the Ni_1 spins could not change their directions near SF1_c, due to the relatively weak exchange interaction of Ni_2 spins. Meanwhile, the $\Delta P_c(H)$ still follows the quadratic relation until the high-field spin-flop transition at H_{high}, indicating that the magnetic point group in the SF1_c does not change at all ($mm2'$). At least it is reasonable to speculate that AFM interaction should be dominated below H_{high}. Here we recall that similar behavior was once reported in Ni_3TeO_6 [13], which exhibits different ME responses to the magnetic fields thanks to the Ni ions carrying different moments. In this case, the Ni_1 spins keep the AFM arrangement along c axis, while Ni_2 spins are still of the AFM order but perpendicular to the c axis, as featured on the top of Fig. 4(a). When the system enters into the SF2_c phase, all the Ni_1 spins rotate towards the direction in perpendicular to the c axis while the Ni_2 spins prefer the ferromagnetic arrangement along the c axis, as the ME coupling is of the linear dependence, thus changing $2'$ to 2. In this way, the magnetic point group in the SF2_c phase could be $mm2$, which allows the first order ME tensor α_{33}, concomitant with our experimental results.

Second, for the $H//a$ case, similarly, only the Ni_2 spins change their direction to be perpendicular to the a axis with the AFM interaction in the SF1_a phase. Because the polarization $\Delta P_c(H)$ in the ground state keeps the same quadratic relation, the $mm2'$ for the SF1_a can be safely assumed. Eventually the Ni_2 spins would rotate to the field direction in the SF2_a phase, and the Ni_1 spins have canted moments along the a axis, resulting in the canted ferromagnetic arrangement, as featured on the top of Fig. 4(c) In this case, the second mirror symmetry m (including the y axis) changes into m', while $2'$ keeps unchanged due to the AFM interaction along c axis. Therefore, the magnetic point group of SF2_a phase is $mm'2'$, which allows the first order ME tensor α_{31}, perfectly verified by our experimental results.

Based on the analysis of the magnetic structures, one is allowed to determine which magnetoelectric coupling mechanism is dominated upon the low-field and high-field SF transitions. When the field $H < H_{\text{high}}$, the magnetic point group does not change with $H//a$ and $H//c$, and noncollinear AFM magnetic structure dominates in the SF1_a and SF1_c phases. Subsequently, the c-axis spontaneous polarization can be reserved due to the DM interaction, see Fig. 8(b). On the other side, Even though it was reported that there might be a slight distortion of the octahedral and tetrahedral coordination environments from the ideal single ion crystal field to the symmetry-adapted, spin-orbit-coupled regime [21], such distortion is very weak that no evident rotation of tilting are detected as shown in the refined neutron scattering at 15 and 1.5 K. Therefore, the net polarization induced by the *p-d* hybridization mechanisms would be zero if the Ni_1 moment on the tetrahedral site is along the c direction or in the ab plane. In this case, due to the noncollinear arrangement of Ni_1 spins, nonzero polarization could be observed, thus giving rise to both c-axis and a-axis polarization.

Second, for the field $H > H_{\text{high}}$, no matter $H//a$ or $H//c$, the spin-current model is no longer applicable to explain the emergence of polarization. Nevertheless, the *p-d* hybridization mechanism may apply, depending on the direction of magnetic field. In the case of $H//c$, the Ni_1 spins are perpendicular to the c axis and Ni_2 spins are a ferromagnetic arrangement along the c axis, thus there is no net polarization for SF2_c phase. Therefore, it is reasonable to ascribe the experimental observed polarization as the consequence of the exchange striction, as that in $\text{Fe}_2\text{Mo}_3\text{O}_8$ For the case of $H//a$, the Ni_1 spins on the tetrahedral site can induce both the c-axis and a-axis polarization components, due to the *p-d* hybridization, while the collinear exchange striction generates the a-axis polarization.

To summarize, we are allowed to propose that the magnetic point groups of SF1_c, SF2_c, SF1_a, and SF2_a phases are $mm2'$, $mm2$, $mm2'$, and $mm'2'$, noting that $mm2'$ only allows the second-order ME tensor. On the contrary, $mm2$ and $mm'2'$ allow the first-order tensor α_{33} and α_{31}, respectively, while both of them allow the second-order tensor, consistent with our experimental results. In addition, it seems that the speculated magnetic structures can explain well the observed magnetization curves and ME effects. The c-axis ME coupling effect can be well explained by combination of spin-current, *p-d* hybridization, and exchange striction mechanisms, based on the low-field and high-field magnetic structures. Surely neutron scattering under magnetic field or reliable theoretical calculations are highly recommended to provide a clean identification of which mechanism or combined mechanisms are responsible for the observed spontaneous polarization and ME effects in $Ni_2Mo_3O_8$, in the future.

V. CONCLUSION

In conclusion, we have presented our systematic investigation on the multiferroic behaviors and ME responses of $Ni_2Mo_3O_8$ single crystals with a noncollinear-ordered spin-1 honeycomb lattice. The unambiguous magnetism-driven ferroelectricity behaviors have been demonstrated by the spontaneous ferroelectric polarization associated with the specific AFM ordering, as well as the quadratic ME response in the low-field region and linear ME response in the high-field region up to 60 T. In particular, the distinctly different ME responses to the in-plane and out-of-plane aligned magnetic fields reflect the characteristics of the polar magnetic symmetry and polar lattice symmetry. More intriguingly, the extraordinarily broad 1/2-like magnetization plateau against the *c*-axis aligned high magnetic field correlates the very different ME responses along the *c* axis and *a* axis. Both the spin-current model and *p*-*d* hybridization mechanism can be applied to explain the observed ferroelectric behaviors and ME responses, consistent with the symmetry-related local ME tensor analysis. The present works indicates that $Ni_2Mo_3O_8$ is a peculiar multiferroic, which provides a perfect platform to explore the rich physics of spin-1 on the honeycomb lattice. Further works, such as electromagnon resonance or nonreciprocal directional dichroism by terahertz (THz) spectroscopy, dynamic behavior of the magnetic moment under different magnetic fields via magnetic torque, and THz absorption spectroscopy measurements, *ab initio* calculations, or mean-field model, are highly recommended to unveil the ME origins as well as the hidden rich physics in this material.

ACKNOWLEDGMENTS

This work was financially supported by the National Key Research Program of China (Grant No. 2016YFA0300101) and the National Science Foundation of China (Grants No. 11874031, No. 11834002, No. 11947092, No. 11774106, No. 51721001, and No. 11974167).

[1] S.-W. Cheong and M. Mostovoy, Multiferroics: A magnetic twist for ferroelectricity, Nat. Mater. **6**, 13 (2007).

[2] T. Kimura, T. Goto, H. Shintani, K. Ishizuka, T.-H. Arima, and Y. Tokura, Magnetic control ferroelectric polarization, Nature (London) **426**, 55 (2003).

[3] M. Fiebig, T. Lottermoser, D. Meier, and M. Trassin, The evolution of multiferroics, Nat. Rev. Mater. **1**, 16046 (2016).

[4] S. Dong, J.-M. Liu, S.-W. Cheong, and Z. Ren, Multiferroic materials and magnetoelectric physics: Symmetry, entanglement, excitation, and topology, Adv. Phys. **64**, 519 (2015).

[5] S. Seki, X. Z. Yu, S. Ishiwata, and Y. Tokura, Observation of skyrmions in a multiferroic material, Science **336**, 198 (2012).

[6] T. Choi, Y. Horibe, H. T. Yi, Y. J. Choi, W. Wu, and S.-W. Cheong, Insulating interlocked ferroelectric and structural antiphase domain walls in multiferroic $YMnO_3$, Nat. Mater. **9**, 253 (2010).

[7] D. I. Khomskii, Electric dipoles on magnetic monopoles in spin ice, Nat. Commun. **3**, 904 (2012).

[8] N. A. Spaldin, M. Fiebig, and M. Mostovoy, The toroidal moment in condensed-matter physics and its relation to the magnetoelectric effect, J. Phys. Condens. Matter **20**, 434203 (2008).

[9] S. K. Yu, B. Gao, J. W. Kim, S.-W. Cheong, M. K. L. Man, J. Madéo, K. M. Dani, and D. Talbayev, High-Temperature Terahertz Optical Diode Effect without Magnetic Order in Polar $FeZnMo_3O_8$, Phys. Rev. Lett. **120**, 037601 (2018).

[10] T. Kurumaji, Y. Takahashi, J. Fujioka, R. Masuda, H. Shishikura, S. Ishiwata, and Y. Tokura, Optical Magnetoelectric Resonance in a Polar Magnet $(Fe, Zn)_2Mo_3O_8$ with Axion-Type Coupling, Phys. Rev. Lett. **119**, 077206 (2017).

[11] T. Kimura, J. C. Lashley, and A. P. Ramirez, Inversion-symmetry breaking in the noncollinear magnetic phase of the triangular-lattice antiferromagnetic $CuFeO_2$, Phys. Rev. B **73**, 220401(R) (2006).

[12] J. F. Wang, M. Tokunaga, Z. Z. He, J. I. Yamaura, A. Matsuo, and K. Kindo, High magnetic field induced phases and half-magnetization plateau in the $S = 1$ kagome compound $Ni_3V_2O_8$, Phys. Rev. B **84**, 220407(R) (2011).

[13] J. W. Kim, S. Artyukhin, E. D. Mun, M. Jaime, N. Harrison, A. Hansen, J. J. Yang, Y. S. Oh, D. Vanderbilt, V. S. Zapf, and S.-W. Cheong, Successive Magnetic Field-Induced Transition and Colossal Magnetoelectric Effect in Ni_3TeO_6, Phys. Rev. Lett. **115**, 137201 (2015).

[14] K. J. Yoo, B. Koteswararao, J. H. Kang, A. Shahee, W. Y. Nam, F. F. Balakirev, V. S. Zapf, N. Harrison, A. Guda, N. T. Oganessian, and K. H. Kim, Magentic field-induced ferroelectricity in $S = 1/2$ Kagome staircase compound $PbCu_3TeO_7$, npj Quant. Mater. **3**, 45 (2018).

[15] E. A. Zvereva, M. I. Stratan, Y. A. Ovchenkov, V. B. Nalbandyan, J.-Y. Lin, E. L. Vavilova, M. F. Iakovleva, M. Abdel-Hafiez, A. V. Silhanek, X.-J. Chen, A. Stroppa, S. Picozzi, H. O. Jeschke, R. Valenti, and A. N. Vasiliev, Zigzag antiferromagnetic quantum ground state in monoclinic honeycomb lattice antimonates $A_3Ni_2SbO_6$ (A = Li, Na), Phys. Rev. B **92**, 144401 (2015).

[16] P. H. Y. Li, R. F. Bishop, D. J. J. Farnell, and C. E. Campbell, Phase diagram of a frustrated Heisenberg antiferromagnet on the honeycomb lattice: The J_1-J_2-J_3 model, Phys. Rev. B **86**, 144404 (2012).

[17] R. Berthelot, W. Schmidt, A. W. Sleight, and M. A. Subramanian, Studies on solid solutions based on layered honeycomb-ordered phases P_2-$Na_2M_2TeO_6$ (M = Co, Ni, Zn), J. Solid State Chem. **196**, 225 (2012).

[18] E. S. Klyushina, B. Lake, A. T. M. N. Islam, J. T. Park, A. Schneidewind, T. Guidi, E. A. Goremychkin, B. Klemke, and M. Månsson, Investigation of the spin-1 honeycomb antiferromagnet $BaNi_2V_2O_8$ with easy-plane anisotropy, Phys. Rev. B **96**, 214428 (2017).

[19] N. D. Khanh, N. Abe, H. Sagayama, A. Nakao, T. Hanashima, R. Kiyanagi, Y. Tokunaga, and T. Arima, Magnetoelectric coupling in the honeycomb antiferromagnet $Co_4Nb_2O_9$, Phys. Rev. B **93**, 075117 (2016).

[20] A. Maignan and C. Martin, $Fe_4Nb_2O_9$: A magnetoelectric antiferromagnet, Phys. Rev. B **97**, 161106(R) (2018).

[21] J. R. Morey, A. Scheie, J. P. Sheckelton, C. M. Brown, and T. M. McQueen, $Ni_2Mo_3O_8$: Complex antiferromagnetic order on a honeycomb lattice, Phys. Rev. Mater. **3**, 014410 (2019).

[22] S. P. McAlister and P. Strobel, Magnetic order in $M_2Mo_3O_8$ single crystals (M = Mn, Fe, Co, Ni), J. Magn. Magn. Mater. **30**, 340 (1983).

[23] I. V. Solovyev and S. V. Streltsov, Microscopic toy model for magnetoelectric effect in polar $Fe_2Mo_3O_8$, Phys. Rev. Mater. **3**, 114402 (2019).

[24] J. S. Wen, S. L. Yu, S. Y. Li, W. Q. Yu, and J. X. Li, Experimental identification of quantum spin liquids, npj Quant. Mater. **4**, 12 (2019).

[25] A. Biffin, R. D. Johnson, I. Kimchi, R. Morris, A. Bombardi, J. G. Analytis, A. Vishwanath, and R. Coldea, Noncoplanar and Counterrotating Incommensurate Magnetic Order Stabilized by Kitaev Interactions in γ-Li_2IrO_3, Phys. Rev. Lett. **113**, 197201 (2014).

[26] J. Chaloupka, G. Jackeli, and G. Khaliullin, Zigzag Magnetic Order in the Iridium Oxide Na_2IrO_3, Phys. Rev. Lett. **110**, 097204 (2013).

[27] T. Kurumaji, S. Ishiwata, and Y. Tokura, Doping-Tunable Ferrimagnetic Phase with Large Linear Magnetoelectric Effect in a Polar Magnet $Fe_2Mo_3O_8$, Phys. Rev. X **5**, 031034 (2015).

[28] Y. Z. Wang, G. L. Pascut, B. Gao, T. A. Tyson, K. Haule, V. Kiryukhin, and S.-W. Cheong, Unveiling hidden ferrimagnetism and giant magnetoelectricity in polar magnet $Fe_2Mo_3O_8$, Sci. Rep. **5**, 12268 (2015).

[29] T. Kurumaji, S. Ishiwata, and Y. Tokura, Diagonal magnetoelectric susceptibility and effect of Fe doping in the polar ferrimagnet $Mn_2Mo_3O_8$, Phys. Rev. B **95**, 045142 (2017).

[30] Y. S. Tang, S. M. Wang, L. Lin, C. Li, S. H. Zheng, C. F. Li, J. H. Zhang, Z. B. Yan, X. P. Jiang, and J.-M. Liu, Collinear magnetic structure and multiferroicity in the polar magnet $Co_2Mo_3O_8$, Phys. Rev. B **100**, 134112 (2019).

[31] S.-W. Cheong, SOS: Symmetry-operational similarity, npj Quant. Mater. **4**, 53 (2019).

[32] P. Strobel, Y. Le Page, and S. P. McAlister, Growth and physical properties of single crystals of $Fe^{II}_2Mo^{IV}_3O_8$, J. Solid State Chem. **42**, 242 (1982).

[33] P. Strobel and Y. L. Page, Growth and morphology of single crystals of hexagonal molybdates $M_2Mo_3O_8$ (M = Mn, Fe, Co, Ni), J. Crys. Growth **61**, 329 (1983).

[34] L. Lin, H. X. Zhu, X. M. Jiang, K. F. Wang, S. Dong, Z. B. Yan, Z. R. Yang, J. G. Wan, and J.-M. Liu, Coupled ferroelectric polarization and magnetization in spinel $FeCr_2S_4$, Sci. Rep. **4**, 6530 (2014).

[35] A. Tari, *The Specific Heat of Matter at Low Temperatures* (Imperial College Press, London, 2003).

[36] H. Ishikawa, M. Yoshida, K. Nawa, M. Jeong, S. Krämer, M. Horvatić, C. Berthier, M. Takigawa, M. Akaki, A. Miyake, M. Tokunaga, K. Kindo, J. Yamaura, Y. Okamoto, and Z. Hiroi, One-Third Magnetization Plateau with a Preceding Novel Phase in Volborthite, Phys. Rev. Lett. **114**, 227202 (2015).

[37] M. A. Khan, Q. Zhang, J.-K. Bao, R. S. Fishman, A. S. Botana, Y. Choi, G. Fabbris, D. Haskel, J. Singleton, and J. F. Mitchell, Steplike metamagnetic transitions in a honeycomb lattice antiferromagnet $Tb_2Ir_3Ga_9$, Phys. Rev. Materials **3**, 114411 (2019).

[38] Y. H. Matsuda, N. Abe, S. Takeyama, H. Kageyama, P. Corboz, A. Honecker, S. R. Manmana, G. R. Foltin, K. P. Schmidt, and F. Mila, Magnetization of $SrCu_2(BO_3)_2$ in Ultrahigh Magnetic Fields Up to 118 T, Phys. Rev. Lett. **111**, 137204 (2013).

[39] R. Chen, J. F. Wang, Z. W. Ouyang, Z. Z. He, S. M. Wang, L. Lin, J. M. Liu, C. L. Lu, Y. Liu, C. Dong, C. B. Liu, Z. C. Xia, A. Matsuo, Y. Kohama, and K. Kondo, Magnetic field induced freeoelectricity and half magnetization plateau in polycrystalline $R_2V_2O_7$ (R = Ni, Co), Phys. Rev. B **98**, 184404 (2018).

[40] A. Okutani, T. Kida, Y. Narumi, T. Shimokawa, Z. Honda, K. Kindo, T. Nakano, Y. Nozue, and M. Hagiwara, High-field magnetism of the honeycomb lattice antiferromagnet $Cu_2(pymca)_3(ClO_4)$, J. Phys. Soc. Jpn. **88**, 013703 (2019).

[41] H. Wiegelmann, A. G. M. Jansen, P. Wyder, J.-P. Rivera, and H. Schmid, Magnetoelectric effect of Cr_2O_3 in strong static magnetic fields, Ferroelectrics **162**, 141 (1994).

[42] T. Arima, D. Higashiyama, Y. Kaneko, J. P. He, T. Goto, S. Miyasaka, T. Kimura, K. Oikawa, T. Kamiyama, R. Kumai, and Y. Tokura, Structural and magnetoelectric properties of $Ga_{2-x}Fe_xO_3$ single crystals grown by a floating-zone method, Phys. Rev. B **70**, 064426 (2004).

[43] G. T. Rado and J. M. Ferrari, Linear and bilinear magnetoelectric effects in magnetically biased magnetite (Fe_3O_4), Phys. Rev. B **15**, 290 (1977).

[44] X. Li, M. F. Liu, Y. Wang, L. M. Tian, R. Shi, L. Yang, Q. Y. Pan, J. J. Han, B. Xie, N. Zhao, X. Z. Wang, S. Z. Li, L. Lin, Z. B. Yan, and J. M. Liu, Magnetoelectric mutual-control in collinear antiferromagnetic $NdCrTiO_5$, Appl. Phys. Lett. **113**, 122903 (2018).

[45] E. Fogh, O. Zaharko, J. Schefer, C. Niedermayer, S. Holm-Dahlin, M. K. Sorensen, A. B. Kristensen, N. H. Andersen, D. Vakinin, N. B. Christensen, and R. Toft-Petersen, Dzyaloshinshii-Moriya interaction and the magnetic ground state in magnetoelectric $LiCoPO_4$, Phys. Rev. B **99**, 104421 (2019).

[46] T. N. Stanislavchuk, G. L. Pascut, A. P. Litvinchuk, Z. Liu, Sungkyun Choi, M. J. Gutmann, B. Gao, K. Haule, V. Kiryukhin, S.-W. Cheong, and A. A. Sirenko, Spectroscopic and first principle DFT+eDMFT study of complex structural, electronic, and vibrational properties of $M_2Mo_3O_8$ (M = Fe, Mn) polar magnets, Phys. Rev. B **102**, 115139 (2020).

[47] T. Kurumaji, Y. Takahashi, J. Fujioka, R. Masuda, H. Shishikura, S. Ishiwata, and Y. Tokura, Electromagnon resonance in a collinear spin state of the polar antiferromagnet $Fe_2Mo_3O_8$, Phys. Rev. B **95**, 020405(R) (2017).

[48] H. Katsura, N. Nagaosa, and A. V. Balatsky, Spin Current and Magnetoelectric Effect in Noncollinear Magnets, Phys. Rev. Lett. **95**, 057205 (2005).

[49] I. A. Sergienko, C. Sen, and E. Dagotto, Ferroelectricity in the Magnetic E-Phase of Orthorhombic Perovskites, Phys. Rev. Lett. **97**, 227204 (2006).

[50] T. Arima, Ferroelectricity induced by proper-screw type magnetic order, J. Phys. Soc. Jpn. **76**, 073702 (2007).

[51] H. J. Xiang, E. J. Kan, Y. Zhang, M. H. Whangbo, and X. G. Gong, General Theory for the Ferromagnetic Polarization

Induced by Spin-Spiral Order, Phys. Rev. Lett. **107**, 157202 (2011).

[52] Y. S. Chai, S. H. Chun, J. Z. Cong, and K. H. Kim, Magnetoelectricity in multiferroic fexaferrites as understood by crystal symmetry analyses, Phys. Rev. B **98**, 104416 (2018).

[53] A. Ruff, P. Lunkenheimer, H. K. von Nidda, S. Widmann, A. Prokofiev, L. Svistov, A. Loidl, and S. Krohns, Chirality-driven ferroelectricity in $LiCuVO_4$, npj Quant. Mater. **4**, 24 (2019).

[54] S. Li, V. Loganathan, and A. H. Nevidomskyy, Noncollinear antiferromagnetic order and effect of spin-orbit coupling in spin-1 honeycomb lattice, arXiv:1906.02215.